ACS Catalysis

pubs.acs.org/acscatalysis

Research Article

Rational Synthesis of Polymeric Nitrogen N_8^- with Ultraviolet Irradiation and Its Oxygen Reduction Reaction Mechanism Study with In Situ Shell-Isolated Nanoparticle-Enhanced Raman Spectroscopy

Zhenhua Yao, Zhiyi Wu, Maocong Hu, Safa Alzaim, Joshua Young, Jinchao Dong, Jinfa Chang, Haizheng Zhuang, El Mostafa Benchafia, Yang Yang, Jianfeng Li, Zafar Iqbal, and Xianqin Wang*

Cite This: *ACS Catal.* 2021, 11, 13034–13040

Read Online

ACCESS | Metrics & More | Article Recommendations | Supporting Information

ABSTRACT: Polynitrogen (PN) deposited on multiwalled carbon nanotubes was synthesized by cyclic voltammetry with ultraviolet (UV) irradiation. Compared to the sample formed without UV, a larger amount of N_8^- was synthesized and was found to distribute more uniformly on the MWNTs with 254 nm UV irradiation, indicating that the production of more azide $(N_3)^0$ radicals as the precursors for synthesis of N_8^- by photoexcitation of azide (N_3^-) ions is a rate-limiting step for PN synthesis. An oxygen reduction reaction kinetics study indicated a four-electron reaction pathway on N_8^-, whereas a two-electron process occurs on N_3^-. Analysis by in situ shell-isolated nanoparticle-enhanced Raman spectroscopy revealed that the side-on and end-on O_2 adsorption occurred at N_8^- and N_3^-, respectively, confirming the electron transfer process. A full direct-methanol fuel cell study shows that methanol crossover typically reduces the current density of Pt/C by ∼40% but has very little effect on the performance of the PN-MWNT catalyst after testing for 120 h. Moreover, the power density from the PN-MWNT cathode is at least twice that from a Pt/C cathode.

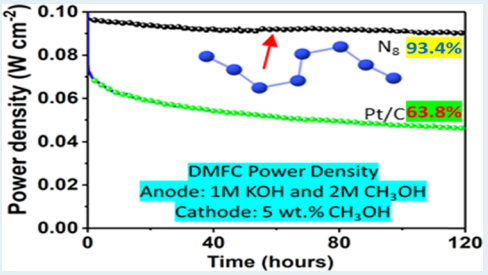

KEYWORDS: *polynitrogen, UV radiation, rate-limiting step, direct-methanol fuel cell, SHINERS*

INTRODUCTION

Direct-methanol fuel cells (DMFCs) for power applications are of great interest due to the ease of transportation of their energy-dense and stable methanol fuel, but their low fuel cell efficiency (∼10%) limits their wide application as a power source for the general energy transport medium.[1] One major challenge is finding an appropriate cathode material, which must exhibit: (1) high activity toward the oxygen reduction reaction (ORR), (2) low activity toward the methanol oxidation reaction (MOR) resulting from methanol crossover, and (3) low cost; such a methanol-tolerant and highly active nonprecious metal catalyst would be critical for improving the efficiency and reducing the expense of DMFCs.[2] However, the nearly four-decade-long search for such electrocatalysts has so far revealed very few materials with promising activity using either fundamental or fuel cell studies.[3]

A promising family of materials are polynitrogen (PN) species and compounds, which are chainlike arrangements of nitrogen atoms that are building blocks for three-dimensional crystalline structures.[2] Pure PN solids are particularly attractive because of their high energy density and decomposition to an inert gas that is nontoxic and friendly to the environment. Motivations of searching for these PN compounds have been for their potential use as highly energetic materials.[3] Recently, a single, zigzag N_8 chain of nitrogen atoms was theoretically shown to be stable inside carbon nanotubes and between sheets of graphene and experimentally synthesized under ambient conditions.[3] Our preliminary work showed that N_8^- is very promising for ORR, which is a sluggish and challenging reaction for DMFC operation.[3] Rational control of the desired N_8^- active species synthesis is critical for achieving better ORR performance. One strategy to increase the amount of N_8^- synthesized is to apply Le Chatelier's principle and increase the concentration of azide ions (N_3^-) during synthesis. However, this strategy is limited to the solubility of azide ions in water. In addition to increasing the precursor concentration, accelerating the rate-limiting step with UV irradiation may also be used to produce azide radicals from azide anions, and the azide radicals may be the critical precursors for the synthesis of N_8^-. Production of N_3^0 radicals by photolysis of sodium azide solution was reported previously.[4,5] Subsequently, Hayon and Simic discussed the possibility of forming unstable N_6 or N_4

Received: July 10, 2021
Revised: September 27, 2021
Published: October 13, 2021

https://doi.org/10.1021/acscatal.1c03102
ACS Catal. 2021, 11, 13034–13040

radicals in solution by reaction of two N_3 neutral radicals produced by photolysis.[6] A more recent study has suggested that various all-nitrogen materials might be obtained by photoexcitation of sodium azide under high pressure.[7] Except for sodium azide, photolysis of other nitrogen precursors such as HN_3,[8] ClN_3,[9] and solid N_2[10] have also been reported and linear N_3, cyclic N_3, N, and N_4 radicals were detected. These results prompted us to accelerate N_8^- synthesis with UV irradiation. The ORR mechanism and methanol crossover effect are critical to develop the PN catalytic materials and are investigated here.

SYNTHESIS OF THE CATALYST

During N_8^- synthesis, dissolved azide ions are oxidized to form azide radicals. N_8^- can be synthesized by further reaction of these radicals and stabilized on the positively charged MWNTs. The reaction route can be denoted as: $N_3^- \rightarrow N_3^{\cdot} \rightarrow N_8^-$. To choose the suitable UV wavelength for the investigation, time-dependent density functional theory (TDDFT) was carried out to obtain the UV−visible absorption spectrum of azide anions in the gas phase (Figure S1).[11]

In this study, a 254 nm mercury lamp (UVP R-52 g, power: 100 W) was used for investigation of the effect of UV irradiation, as the 254 nm mercury line lies in the absorption band with the highest intensity near the 250 nm region (Figure S1).[11] For comparison, a 365 nm mercury lamp (UVP B-100AR, power: 100 W) was also used, and the light emitted is not absorbed by the azide solution. UV absorption at higher energy (145−150 nm) might produce more active azide radicals. However, because UV radiation with a wavelength below 200 nm can be strongly absorbed by oxygen in air[12] or water[13] in the solution, it was not investigated in this study.

PN-MWNT sheets and PN-MWNTs on a glassy carbon electrode (GCE) were synthesized under UV irradiation during cyclic voltammetry (CV), and the resulting samples are denoted as PN-MWNT sheet 254 nm, PN-MWNT-GCE 254 nm, PN-MWNT sheet 365 nm, and PN-MWNT-GCE 365 nm, respectively, which corresponded to the wavelength of the UV irradiation used. MWNT sheets were used to synthesize PN-MWNT sheets with or without UV to produce a large amount of PN-MWNT sheet samples for the following characterizations: Raman spectroscopy, Fourier transform infrared (FTIR) spectroscopy, and temperature programmed desorption (TPD). The CV synthesis curves with the GCE are shown in Figures S2−S4. During each cycle, an anodic peak was detected for each sample between 0.5 and 0.6 V, which can be assigned to the oxidation of azide ions. Without UV or with UV irradiation at 365 nm during synthesis, the overall trend for the anodic current density within the 12 cycles decreased continuously due to the decreased surface N_3^- concentration on the MWNTs during CV synthesis. However, with 254 nm UV irradiation there was no obvious trend for the anodic current density, and it is possibly because photoexcitation of the azide ions by UV irradiation at 254 nm produced more N_3^0 radicals for the subsequent electrochemical oxidation process, which compensated for the decrease in N_3^- concentration during synthesis. Moreover, it can be found that the cycle 4 of the 254 nm sample, which had the lowest oxidation current density, was close to that of cycle 1 of the sample without UV, which had the highest oxidation current density, and much higher than that of the cycle 1 of the sample with UV irradiation at 365 nm, which also had the highest oxidation current density. Therefore, the current density of the oxidation peak followed the trend: PN-MWNT-GCE 254 nm > PN-MWNT-GCE > PN-MWNT-GCE 365 nm. It is therefore clear that more azide ions were oxidized with 254 nm UV irradiation compared to the sample with UV irradiation at 365 nm or without UV irradiation. The temperature of the electrolytes was also measured during the synthesis (Figure S5). The results showed that while both the 254 and 365 nm UV irradiations heated the electrolytes, the 365 nm UV irradiation produced more heat. The lower anodic current density of the sample with 365 nm UV irradiation than the sample without UV was possibly because 365 nm UV radiation is not absorbed by the azide ions, while heating caused the formation and evaporation of HN_3 from the acidic electrolyte such that less azide ions could diffuse to the surface of the MWNT electrode to be oxidized (for more details see the Supporting Information Materials and Methods section and Figure S6).

CHARACTERIZATION OF THE CATALYST SYNTHESIS PRODUCTS

To identify the products after PN-MWNT sheet synthesis with UV irradiation, Raman spectroscopy was carried out and the results are shown in Figure 1A. The vibrational mode at 1080 cm^{-1} was detected from the PN-MWNT sheet and PN-MWNT sheet irradiated with 254 nm, which can be assigned to N_8^{-3}. However, the line was barely detectable from the PN-MWNT sheet irradiated at 365 nm, which suggested that much less N_8^- was synthesized. ATR-FTIR spectra in Figure 1B show a clear line at about 2050 cm^{-1}, which can be assigned to N_8^{-3}, and the peak intensity corresponding to the amount of N_8^- synthesized increased in the following order: PN-MWNT sheet irradiated at 254 nm > PN-MWNT unirradiated sheet > PN-MWNT sheet irradiated at 365 nm. The line near 2100 cm^{-1} can be assigned to the azide ion asymmetric stretching mode from unreacted sodium azide,[3] and the peak intensity corresponding to the residual N_3^- amount showed the following order: PN-MWNT sheet irradiated at 365 nm > PN-MWNT unirradiated sheet > PN-MWNT sheet irradiated at 254 nm. The lines around 1500, 1640, and 3300 cm^{-1} can be assigned to the residual water trapped in the MWNT sheets. To investigate the thermal stability of the PN samples, TPD was carried out for different samples and the results are shown in Figure 1C. Nitrogen desorption due to decomposition of N_8^- was detected between 400 and 450 °C. The amount of nitrogen desorbed suggested that synthesis of N_8^- was significantly increased by UV irradiation at 254 nm, while a smaller amount of N_8^- was synthesized with UV irradiation at 365 nm, compared to the sample that was not irradiated with UV. The desorption peak from the PN-MWNT irradiated at 254 nm sample was much narrower than that from the PN-MWNT sample, which suggested that the N_8^- synthesized under irradiation was more uniformly deposited on the MWNT sheet. The Raman, FTIR, and TPD results are consistent with the CV synthesis results and further confirm that the amount of N_8^- synthesized is enhanced with 254 nm UV irradiation, most likely because absorption of the 254 nm UV radiation facilitates the rate-limiting step of the synthesis, which is the electrochemical oxidation of azide ions to azide N_3^0 radicals. The 365 nm UV radiation cannot be absorbed by the azide ions, and heating by a UV lamp may further inhibit adsorption of azide species and increase the desorption of the final product, thus leading to a smaller amount of N_8^- being synthesized on the substrate.

https://doi.org/10.1021/acscatal.1c03102
ACS Catal. 2021, 11, 13034−13040

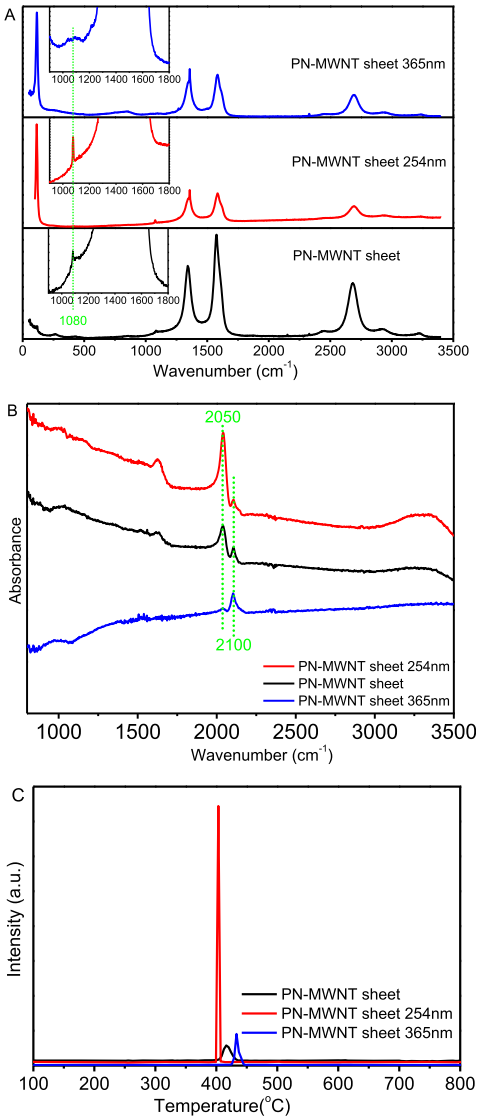

Figure 1. Characterization of PN samples. (A) Raman spectra using 10 mW 514.5 nm laser excitation. (B) ATR-FTIR spectra. The MWNT background has been subtracted from the samples. (C) N^{14} signal from TPD scans. The curves have been normalized by the sample weight.

ELECTROCATALYTIC ACTIVITY OF THE SYNTHESIZED CATALYST

The electrocatalytic activities of the as-prepared PN-MWNT-GCEs toward ORR were evaluated by LSV (linear sweep voltammetry) measurements using a rotating disk electrode (RDE) setup at different rotating speeds in O_2-saturated 0.1 M KOH electrolyte at a scan rate of 5 mVs^{-1}. As can be seen in Figure 2A–C, the catalytic current density for all three samples increased with increasing rotating speed due to the enhanced diffusion of the electrolytes.[14] In addition, the current density increased with the following trend: PN-MWNT-GCE irradiated at 254 nm > PN-MWNT-GCE unirradiated > PN-MWNT-GCE irradiated at 365 nm (Figure 2D). This current density trend is consistent with that for the synthesized amount of N_8^- indicated by the Raman, FTIR, and TPD results, suggesting that the larger amounts of N_8^- formed on the MWNTs lead to higher reduction current densities. Furthermore, the current density of the PN-MWNT-GCE

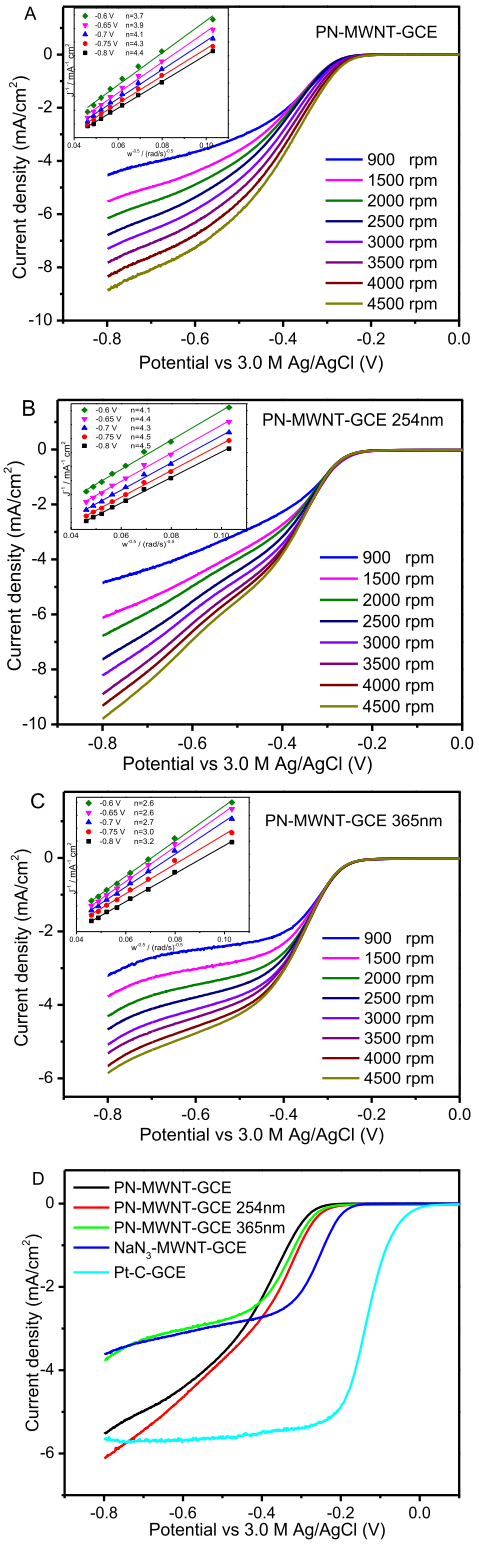

Figure 2. LSV curves of ORR on (A) PN-MWNT-GCE, (B) PN-MWNT-GCE 254 nm, and (C) PN-MWNT-GCE 365 nm in an oxygen-saturated 0.1 M KOH solution with different rotation rates (scan rate: 5 mV/s). The insets in A, B, and C show corresponding Koutecky–Levich plots (1/J vs $1/\omega^{0.5}$). LSV curves of ORR on (D) PN-MWNT-GCE, PN-MWNT-GCE 254 nm, PN-MWNT-GCE 365 nm, NaN_3-MWNT-GCE, and Pt-C-GCE in an oxygen-saturated 0.1 M KOH solution with a rotation speed of 1500 rpm (scan rate: 5 mV/s).

https://doi.org/10.1021/acscatal.1c03102
ACS Catal. 2021, 11, 13034–13040

sample irradiated at 254 nm was even higher than that of the commercial Pt/C-GCE catalyst at a potential of −0.8 V [10% platinum on Vulcan XC-72 (E-Tek)], see Figure S7A. Moreover, it is worth noting that the percentage of nitrogen loading in the PN-MWNT-GCE sample irradiated at 254 nm (5.46 wt %.) was determined by TPD using the same approach reported in our previous work.[3] Lower ORR current densities were obtained on NaN_3 and PN with the temperature effect (Figure S7B,C).

The kinetics of the ORR process was evaluated by employing the Koutecky−Levich (K−L) equation (see the Supporting Information for details).[15,16] Before conducting a fitting analysis for the PN samples, the transferred electron number (n) per oxygen molecule on the commercial Pt/C catalyst was derived via the K−L equation to be 4.4−4.5 (Figure S8A) suggesting a four-electron process on the Pt/C electrode as shown, which confirmed the reliability of the data collected and validity of the fitting method.[17,18] The K−L plots of $1/J$ vs $1/\omega^{0.5}$ for all three PN samples are displayed in Figure 2A−C insets. All fitting lines of the samples gave good linearity and were parallel, indicating a first-order reaction with dissolved oxygen.[19] Moreover, the n value at the PN-MWNT-GCE was derived to be 3.7−4.4, which indicated that a four-electron process on N_8 [14,19] is involved. Similar n values in the 4.1−4.5 range was achieved on the sample PN-MWNT-GCE irradiated at 254 nm (Figure S8C), which suggested that the reaction pathway for this sample was also through a dominant four-electron process. However, the n value for PN-MWNT-GCE irradiated at 365 nm was in the 2.6−3.2 range, lying between the two-electron and four-electron reduction processes, suggesting that ORR proceeds by a coexisting pathway involving both the two-electron and four-electron transfer processes.[20] ORR on N_3^- follows a two-electron pathway, while on N_8 it is through a four-electron pathway (as proven by PN-MWNT-GCE results) in consideration of coexistence of a large amount of residual N_3^- and a small amount of N_8 produced on PN-MWNT-GCE irradiated at 365 nm as concluded by the FTIR and Raman results. To confirm this assumption, the same LSV measurement was performed on the N_3^--MWNT-GCE. The N_3^--MWNT-GCE was prepared by dipping the MWNT-GCE in the 2 M NaN_3 electrolyte for 11 h followed by further drying in air overnight. The ORR polarization curves and fitting results are shown in Figures S7B and S8B. The derived n value for the N_3^--MWNT-GCE was 2.4−2.9, which led to a characteristic two-electron process and further confirmed the aforementioned hypothesis.

MECHANISM OF CATALYST ACTIVITY BY IN SITU NANOPARTICLE-ENHANCED RAMAN SPECTROSCOPY AND DENSITY FUNCTIONAL THEORY

The different transferred electron numbers derived in the above kinetics study indicated that the mechanisms involved are different. One of the widely adopted approaches to explore the mechanism of ORR is to probe the O_2 chemisorption mode on the catalyst which was originally proposed by Gong et al.[27] through combining experiments with density functional theory (DFT) calculations. Their theoretical work revealed that the side-on adsorption (Yeager model) favored the four-electron pathway while the end-on adsorption (the Pauling model) led to a two-electron process on the Pt electrode. In this study, the O_2 chemisorption mode was determined by in situ shell-isolated nanoparticle-enhanced Raman spectroscopy (SHINERS)[21−24] by monitoring the surface reaction process. Most recently, Galloway and Hardwick[22] utilized SHINERS for the same reaction on a Pt electrode and they assigned lines centered at 456 and 490 cm^{-1} to the O_2 modes associated with the O_2 flat (or side-on) and end-on adsorption orientations, respectively. Figure 3A,B presents the in situ SHINERS spectra

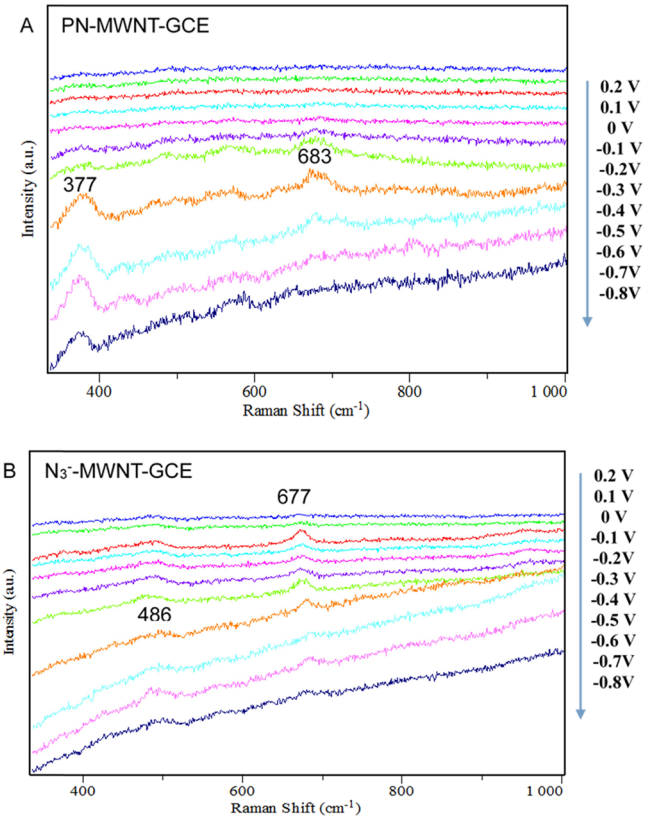

Figure 3. In situ SHINERS spectra of ORR on (A) PN-MWNT-GCE and (B) N_3^--MWNT-GCE.

of ORR on PN-MWNT-GCE and N_3^--MWNT-GCE. On the PN-MWNT-GCE surface, two lines are observed at 377 and 683 cm^{-1}, respectively, at different potentials. The former line can be attributed to the side-on adsorption of O_2, which is close to the reported wavenumber of the side-on peak (the small difference may be due to the different catalysts used in the two studies, i.e., PN vs Pt, which suggested that a four-electron pathway is involved. The latter peak can be attributed to a peroxide species.[25] Furthermore, this very weak peak indicates that the quantity of the generated peroxide species is negligible. Therefore, it can be concluded that the dominant pathway on PN-MWNT-GCE is through a four-electron process, which is consistent with the observed n value close to 4 in the kinetics study discussed above. The SHINERS spectra of N_3^--MWNT-GCE also show two lines. The lower wavenumber peak shifts to 486 cm^{-1}, while the higher wavenumber peak almost remains the same (677 cm^{-1}) compared with that of PN. The 486 cm^{-1} line is close to the reported wavenumber of the end-on adsorption peak (490 cm^{-1}) suggesting that the reaction is through the two-electron process. The 677 cm^{-1} line is also assigned to a peroxide species[25] and is significantly stronger compared to that on the

https://doi.org/10.1021/acscatal.1c03102
ACS Catal. 2021, 11, 13034−13040

Table 1. Stable Intermediate Species of ORR on N_8-MWNT-GCE and N_3^--MWNT-GCE and the Comparison of Raman Frequencies

Stable intermediate species from DFT	Calculated frequency (cm^{-1})	Experimental frequency (cm^{-1})	Deviation (%)
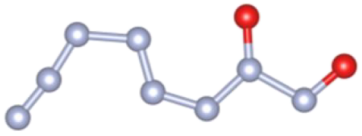 $N_8^-/2O^*$	380.6 687.8	377 683	0.9 0.7
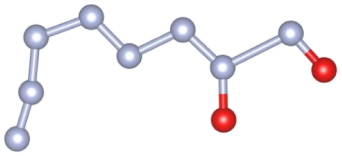 $N_8^0/2O^*$	381.9 687.9	377 683	1.3 0.7
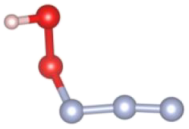 (d) $N_3^0/*OOH$	460.1 673.5	486 677	5.3 0.5

PN sample, indicating that the generated peroxide species was abundant on this sample. Accordingly, the ORR mechanism is via a two-electron process, which further confirms the above kinetics study.

To confirm the SHINERS results, DFT calculations were performed. A (5,5) armchair CNT terminated by H atoms was used, as previous work demonstrated this is an appropriate model for PN systems.[26] An N_8^- molecule was placed on the outside of this CNT, and the entire system was fully optimized. A natural bonding orbital (NBO) analysis (Figure S9) revealed that there existed charge transfer between N_8^- and CNT, with charge decreasing on N_8^-. Thus, the subsequent study of different oxygen species adsorption on both N_8^0 and N_8^- was investigated. All stable configurations and transition states were verified via numerical frequency calculations. Table 1 lists the DFT-determined stable species on the catalyst surface and both calculated and experimental Raman frequencies (full list is given in Table S1). The split 2O* intermediate on N_8^0 and N_8^- shown in Table 1 is highly stable with ($\Delta G[2O^*/N_8^-]$ = −4.56 eV; $\Delta G[2O^*/N_8^0]$ = −2.19 eV) and therefore likely the one detected by SHINERS. Indeed, this split 2O* intermediate shows Raman active modes close to the ones at 377 and 683 cm^{-1} observed in the experimental SHINERS spectrum. The $N_8^0/2O^*$ system has modes at 381.9 and 686.9 cm^{-1}, while the $N_8^-/2O^*$ system has modes at 380.6 and 687.8 cm^{-1} with relatively high Raman activity. These results confirm that the O−O bonding is easily broken on N_8 by this side-on adsorption.[27]

Similar DFT calculations were also performed on N_3^0 neutral and N_3^- anions. N_3 is a linear centrosymmetric species with more negative charge on the two end nitrogen atoms that are more active for oxygen adsorption.[28,29] Split $2O^*/N_3^0$ and $*OOH/N_3^0$ are both highly stable intermediates ($\Delta G[2O^*/N_3^0]$ = −5.53 eV; $\Delta G[*OOH/N_3^0]$ = −4.64 eV). The split $2O^*/N_3^0$ has only one Raman active mode at 664.5 cm^{-1}, while $*OOH/N_3^0$ has two relatively strong modes at 460.1 and 673.5 cm^{-1} (Table S2) that are close to the observed SHINERS peaks at 486 and 677 cm^{-1}. It is therefore likely that the SHINERS peaks arise mainly from $*OOH/N_3^0$. These results agree with the SHINERS analysis that the ORR on the N_3/MWCNT proceeds by the two-electron pathway with production of H_2O_2, through which an OOH intermediate is expected.

The methanol crossover effect of the electrocatalyst should be tested for potential use in DMFCs. Methanol chemisorption on PN and Pt was then compared by DFT calculations by computing the adsorption energy, which was found to be −0.19 and −0.50 eV for N_8^0 and a Pt (100) surface, respectively. This 2.5 times larger adsorption energy further confirms that methanol has a significantly weaker interaction with PN than with a Pt surface. To further confirm methanol tolerance of the PN-MWNT catalyst, the power density was directly measured for 120 h in a full DMFC with 5 wt % methanol on the cathode side and 2 M methanol on the anode side as shown in Figure 4. After testing for 120 h the activity of the cathode with PN-MWNT-GCE-254 nm is retained at ca. 93%; in contrast, the commercial Pt/C just has a retention rate of 63%, indicating the superior stability and methanol tolerance of PN as the cathode. Moreover, the power density using PN-MWNT is twice that of Pt/C.

CONCLUSIONS

A highly active and methanol crossover tolerant electrocatalyst, N_8^-, was synthesized by accelerating the rate-limiting step ($N_3^- \rightarrow N_3^{\cdot}$) with the irradiation using 254 nm UV light. A kinetics study revealed that reduction occurs through a four-electron process at N_8 while the O_2 reduction catalyzed at the N_3^- is a two-electron process, which is consistent with the SHINERS experiments and DFT calculations. Methanol crossover experiments using a full DMFC indicated that N_8

https://doi.org/10.1021/acscatal.1c03102
ACS Catal. 2021, 11, 13034−13040

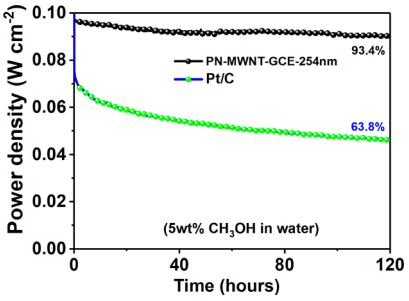

Figure 4. Power density and stability comparison of PN-MWNT-GCE-254 nm and Pt-C-GCE in DMFC tests. The anode is fed with 1 M KOH and 2 M methanol solutions at a flow rate of 20 mL min^{-1}, and the cathode is fed with 100% humidified high purity O_2 (99.99%) at 200 mL min^{-1} without backpressure. O_2 was saturated with a 5 wt % methanol/water mixture.

is more stable and hence more active than the Pt/C commercial catalyst in DMFCs and is a better catalyst for DMFCs.

■ ASSOCIATED CONTENT

Supporting Information

The Supporting Information is available free of charge at https://pubs.acs.org/doi/10.1021/acscatal.1c03102.

The experimental details of material synthesis, characterizations, electrochemical measurement, DMFC test, and DFT calculations, UV−visible absorption spectrum of the azide anion determined by TDDFT (Figure S1), CV curves of 12 cycles for different samples (Figures S2−S4), temperature profiles of the electrolyte during CV synthesis (Figures S5 and S6), LSV curves (Figure S7), Koutecky−Levich plots (Figure S8), NBO partial charge distribution on an N_8^- anion (Figure S9), and calculated vibrational frequencies and Raman activity for O_2 split and *OOH adsorption (Tables S1 and S2) (PDF)

■ AUTHOR INFORMATION

Corresponding Author

Xianqin Wang − *Department of Chemical and Materials Engineering, New Jersey Institute of Technology, Newark, New Jersey 07102, United States;* orcid.org/0000-0003-1056-7214; Phone: +1 973 596 5707; Email: xianqin.wang@njit.edu; Fax: +1 973 596 8436

Authors

Zhenhua Yao − *Department of Chemical and Materials Engineering, New Jersey Institute of Technology, Newark, New Jersey 07102, United States;* Present Address: Key Laboratory of Optoelectronic Chemical Materials and Devices, Ministry of Education, School of Chemical and Environmental Engineering, Jianghan University, Wuhan 430056, China (Z.Y. and M.H.)

Zhiyi Wu − *Department of Chemical and Materials Engineering, New Jersey Institute of Technology, Newark, New Jersey 07102, United States*

Maocong Hu − *Department of Chemical and Materials Engineering, New Jersey Institute of Technology, Newark, New Jersey 07102, United States;* Present Address: Key Laboratory of Optoelectronic Chemical Materials and Devices, Ministry of Education, School of Chemical and Environmental Engineering, Jianghan University, Wuhan 430056, China (Z.Y. and M.H.)

Safa Alzaim − *Department of Chemical and Materials Engineering, New Jersey Institute of Technology, Newark, New Jersey 07102, United States*

Joshua Young − *Department of Chemical and Materials Engineering, New Jersey Institute of Technology, Newark, New Jersey 07102, United States*

Jinchao Dong − *MOE Key Laboratory of Spectrochemical Analysis and Instrumentation, State Key Laboratory of Physical Chemistry of Solid Surfaces, College of Chemistry and Chemical Engineering, Xiamen University, Xiamen 361005, China*

Jinfa Chang − *NanoScience Technology Center, Department of Materials Science and Engineering, Department of Chemistry, Renewable Energy and Chemical Transformation Cluster, University of Central Florida, Orlando, Florida 32826, United States;* orcid.org/0000-0002-5066-3625

Haizheng Zhuang − *Department of Chemical and Materials Engineering, New Jersey Institute of Technology, Newark, New Jersey 07102, United States*

El Mostafa Benchafia − *Interdisciplinary Program in Materials Science and Engineering, New Jersey Institute of Technology, Newark, New Jersey 07102, United States*

Yang Yang − *NanoScience Technology Center, Department of Materials Science and Engineering, Department of Chemistry, Renewable Energy and Chemical Transformation Cluster, University of Central Florida, Orlando, Florida 32826, United States;* orcid.org/0000-0002-4410-6021

Jianfeng Li − *MOE Key Laboratory of Spectrochemical Analysis and Instrumentation, State Key Laboratory of Physical Chemistry of Solid Surfaces, College of Chemistry and Chemical Engineering, Xiamen University, Xiamen 361005, China;* orcid.org/0000-0003-1598-6856

Zafar Iqbal − *Department of Chemical and Materials Engineering, New Jersey Institute of Technology, Newark, New Jersey 07102, United States*

Complete contact information is available at: https://pubs.acs.org/10.1021/acscatal.1c03102

Author Contributions

X.W. conceived and supervised the research and finalized the manuscript. Z.I. helped with the Raman data and the chemistry of the azides and the manuscript. Z.Y., Z.W., and M.H. performed the experiments and interpreted the experimental data. S.A., J.Y., and E.M.B. performed the DFT simulations. J.D. and J.L. collected the SHINERS data. J.C. and Y.Y. collected DMFC data. H.Z. synthesized the PN sample for the DMFC test. Z.Y., Z.W., and M.H. contributed equally.

Funding

This work was financially supported by NSF CBET-1804949.

Notes

The authors declare no competing financial interest.

■ REFERENCES

(1) Su, H.; Hu, Y. H. Recent Advances in Graphene-Based Materials for Fuel Cell Applications. *Energy Sci. Eng.* **2021**, *9*, 958−983.

(2) Ovidiu, P. The Study of the Efficiency of a Direct Methanol Fuel Cell. *J. Electr. Electron. Eng.* **2014**, *7*, 31−34.

(3) Wu, Z.; Benchafia, E. M.; Iqbal, Z.; Wang, X. N_8^- Polynitrogen Stabilized on Multi-Wall Carbon Nanotubes for Oxygen-Reduction Reactions at Ambient Conditions. *Angew. Chem. Int. Ed.* **2014**, *126*, 12763−12767.

(4) Barat, F.; Hickel, B.; Sutton, J. Flash Photolysis of Aqueous Solutions of Azide and Nitrate Ions. *J. Chem. Soc. D* **1969**, 125b−1126b.
(5) Treinin, A.; Hayon, E. Spectroscopic Observation of the Azide Radical in Solution. *J. Chem. Phys.* **1969**, *50*, 538−539.
(6) Hayon, E.; Simic, M. Absorption Spectra and Kinetics of the Intermediate Produced from the Decay of Azide Radicals. *J. Am. Chem. Soc.* **1970**, *92*, 7486−7487.
(7) Peiris, S. M.; Russell, T. P. Photolysis of Compressed Sodium Azide (NaN3) as a Synthetic Pathway to Nitrogen Materials. *J. Phys. Chem. A* **2003**, *107*, 944−947.
(8) Thrush, B. A. The Detection of Free Radicals in the High Intensity Photolysis of Hydrogen Azide. *Proc. R. Soc. London, Ser. A* **1956**, *235*, 143−147.
(9) Hansen, N.; Wodtke, A. M. Velocity Map Ion Imaging of Chlorine Azide Photolysis: Evidence for Photolytic Production of Cyclic-N3. *J. Phys. Chem. A* **2003**, *107*, 10608−10614.
(10) Chou, S.-L.; Lo, J.-I.; Lin, M.-Y.; Peng, Y.-C.; Lu, H.-C.; Cheng, B.-M. Production of N3 upon Photolysis of Solid Nitrogen at 3 K with Synchrotron Radiation. *Angew. Chem. Int. Ed.* **2014**, *53*, 738−741.
(11) Burak, I.; Treinin, A. The Photochemistry of N_3^- in Aqueous Solution at 254 Mμ. *J. Am. Chem. Soc.* **1965**, *87*, 4031−4036.
(12) Thiemens, M. H.; Jackson, T. Production of Isotopically Heavy Ozone by Ultraviolet Light Photolysis of O2. *Geophys. Res. Lett.* **1987**, *14*, 624−627.
(13) Han, W.; Zhu, W.; Zhang, P.; Zhang, Y.; Li, L. Photocatalytic Degradation of Phenols in Aqueous Solution under Irradiation of 254 and 185nm UV Light. *Catal. Today* **2004**, *90*, 319−324.
(14) Jin, H.; Huang, H.; He, Y.; Feng, X.; Wang, S.; Dai, L.; Wang, J. Graphene Quantum Dots Supported by Graphene Nanoribbons with Ultrahigh Electrocatalytic Performance for Oxygen Reduction. *J. Am. Chem. Soc.* **2015**, *137*, 7588−7591.
(15) Lai, L.; Potts, J. R.; Zhan, D.; Wang, L.; Poh, C. K.; Tang, C.; Gong, H.; Shen, Z.; Lin, J.; Ruoff, R. S. Exploration of the Active Center Structure of Nitrogen-Doped Graphene-Based Catalysts for Oxygen Reduction Reaction. *Energy Environ. Sci.* **2012**, *5*, 7936−7942.
(16) Selvakumar, K.; Senthil Kumar, S. M.; Thangamuthu, R.; Ganesan, K.; Murugan, P.; Rajput, P.; Jha, S. N.; Bhattacharyya, D. Physiochemical Investigation of Shape-Designed MnO2 Nanostructures and Their Influence on Oxygen Reduction Reaction Activity in Alkaline Solution. *J. Phys. Chem. C* **2015**, *119*, 6604−6618.
(17) Silva, R.; Voiry, D.; Chhowalla, M.; Asefa, T. Efficient Metal-Free Electrocatalysts for Oxygen Reduction: Polyaniline-Derived N- and O-Doped Mesoporous Carbons. *J. Am. Chem. Soc.* **2013**, *135*, 7823−7826.
(18) Holewinski, A.; Idrobo, J.-C.; Linic, S. High-Performance Ag-Co Alloy Catalysts for Electrochemical Oxygen Reduction. *Nat. Chem.* **2014**, *6*, 828−834.
(19) Li, Y.; Zhao, Y.; Cheng, H.; Hu, Y.; Shi, G.; Dai, L.; Qu, L. Nitrogen-Doped Graphene Quantum Dots with Oxygen-Rich Functional Groups. *J. Am. Chem. Soc.* **2012**, *134*, 15−18.
(20) Wang, S.; Yu, D.; Dai, L. Polyelectrolyte Functionalized Carbon Nanotubes as Efficient Metal-Free Electrocatalysts for Oxygen Reduction. *J. Am. Chem. Soc.* **2011**, *133*, 5182−5185.
(21) Li, C.-Y.; Dong, J.-C.; Jin, X.; Chen, S.; Panneerselvam, R.; Rudnev, A. V.; Yang, Z.-L.; Li, J.-F.; Wandlowski, T.; Tian, Z.-Q. In Situ Monitoring of Electrooxidation Processes at Gold Single Crystal Surfaces Using Shell-Isolated Nanoparticle-Enhanced Raman Spectroscopy. *J. Am. Chem. Soc.* **2015**, *137*, 7648−7651.
(22) Galloway, T. A.; Hardwick, L. J. Utilizing in Situ Electrochemical SHINERS for Oxygen Reduction Reaction Studies in Aprotic Electrolytes. *J. Phys. Chem. Lett.* **2016**, *7*, 2119−2124.
(23) Huang, Y.-F.; Kooyman, P. J.; Koper, M. T. M. Intermediate Stages of Electrochemical Oxidation of Single-Crystalline Platinum Revealed by in Situ Raman Spectroscopy. *Nat. Commun.* **2016**, *7*, 12440.
(24) Li, J.-F.; Anema, J. R.; Wandlowski, T.; Tian, Z.-Q. Dielectric Shell Isolated and Graphene Shell Isolated Nanoparticle Enhanced Raman Spectroscopies and Their Applications. *Chem. Soc. Rev.* **2015**, *44*, 8399−8409.
(25) Dai, W.-L.; Dong, Y.; Cao, Y.; Deng, J.-F.; Fan, K.-N.; Liao, Y.-Y.; Hong, B.-F. In Situ Raman Studies on the Interaction of Oxygen and Methanol with an Iodine-Modified Electrolytic Silver Catalyst. *J. Raman Spectrosc.* **2002**, *33*, 318−324.
(26) Battaglia, S.; Evangelisti, S.; Leininger, T.; Faginas Lago, N. Confinement of the Pentanitrogen Cation Inside Carbon Nanotubes. In *International Conference on Computational Science and Its Applications*; Springer: Cham, 2018; pp. 579-592.
(27) Gong, K.; Du, F.; Xia, Z.; Durstock, M.; Dai, L. Nitrogen-Doped Carbon Nanotube Arrays with High Electrocatalytic Activity for Oxygen Reduction. *Science* **2009**, *323*, 760−764.
(28) Stevens, E. D.; Hope, H. A Study of the Electron-Density Distribution in Sodium Azide, NaN3. *Acta Crystallogr. A* **1977**, *33*, 723−729.
(29) Wang, X.; Li, J.; Zhu, H.; Chen, L.; Lin, H. Polymerization of Nitrogen in Cesium Azide under Modest Pressure. *J. Chem. Phys.* **2014**, *141*, No. 044717.

https://doi.org/10.1021/acscatal.1c03102
ACS Catal. 2021, 11, 13034−13040